

Received January 14, 2019, accepted January 30, 2019, date of publication February 4, 2019, date of current version February 22, 2019.

Digital Object Identifier 10.1109/ACCESS.2019.2897140

Optimization-Based Image Reconstruction From Fast-Scanned, Noisy Projections in EPR Imaging

ZHIWEI QIAO^{ID1}, DONG LIANG^{ID2}, (Senior Member, IEEE), SHAOJIE TANG³, AND HOWARD HALPERN⁴

¹School of Computer and Information Technology, Shanxi University, Taiyuan 030006, China

²The Paul C. Lauterbur Research Center for Biomedical Imaging, Shenzhen Institutes of Advanced Technology, Chinese Academy of Sciences, Shenzhen 518055, China

³School of Automation, Xi'an University of Posts and Telecommunications, Xi'an 710121, China

⁴Department of Radiation and Cellular Oncology, The University of Chicago, Chicago, IL 60637, USA

Corresponding authors: Zhiwei Qiao (zqiao@sxu.edu.cn) and Howard Halpern (hhalpern@uchicago.edu)

This work was supported in part by the Natural Science Foundation of Shanxi Province under Grant 201601D011041, in part by the Shanxi Provincial Key Research and Development Plan under Grant 201803D421012, in part by the Fund Program for the Scientific Activities of Selected Returned Overseas Professionals in Shanxi Province under Grant rsc1622, in part by the Shaanxi Provincial Natural Science Foundation of China under Grant 2016JM8034, and in part by the National Institutes of Health (NIH) under Grant P41 EB002034, Grant R01 CA98575, and Grant R01 CA182264.

ABSTRACT Tumor oxygen concentration image is essential to oxygen-image guided, precise radiation therapy. Electron paramagnetic resonance imaging is an advanced oxygen imaging technique. However, the scanning time is still comparatively long, leading to motion artifacts for static imaging and low time resolution for dynamic imaging. Usually, a projection signal at a specific angle is obtained by averaging thousands of repeatedly collected projections to suppress random noise and achieve a high signal-to-noise ratio (SNR). Reducing the repetition times of projection collecting at a specific angle may effectively speed up the whole scanning process. However, the EPR images reconstructed by the conventional three-dimensional filtered backprojection (FBP) algorithm from these fast-scanned, low SNR projections are too noisy to be used for further image postprocessing. In the paper, we investigate the capability of an optimization-based algorithm in accurate reconstruction from noisy projections. We designed a total variation constrained, data divergence minimization model, derived its Chambolle-Pock (CP) solving algorithm, and then validated and evaluated the CP algorithm via mathematical and physical phantoms. The studies show that the CP algorithm may accurately reconstruct EPR images from fast-scanned, noisy projections, and thus the whole scanning process may be speeded up four times compared with the full scan time demanded by the FBP algorithm in the image reconstruction of the complex physical phantom.

INDEX TERMS Chambolle-Pock (CP) algorithm, electron paramagnetic resonance imaging (EPRI), fast scan, optimization, total variation (TV) minimization.

I. INTRODUCTION

Studies have shown that oxygen concentration in tumor is a key information for effective radiation therapy [1]. Advanced radiation therapy demands that hypoxia (low oxygen concentration) region should be irradiated using high dose ray, whereas high oxygen concentration region is fit for low dose ray. This is because hypoxia is resistant to radiation [2]. Electron Paramagnetic Resonance (EPR) Imaging (EPRI) is an advanced oxygen imaging modality for its higher spatial resolution and oxygen concentration resolution [3], [4].

The associate editor coordinating the review of this manuscript and approving it for publication was Eduardo Rosa-Molinar.

There are two types of EPR oxygen imaging methods: pulsed EPRI [5], [6] and continuous-wave (CW) EPRI [7]. Pulsed EPRI has higher scanning speed than CW EPRI, leading to wider applications to *in vivo* oxygen imaging, especially to tumor-oxygen imaging [8], [9].

Pulsed EPR oxygen imaging method may use the following procedure [3]: (1) Reconstruct 8 T1-weighted unpaired electron spin density (UESD) images; (2) Get the T1 image by fitting the T1 curve for each voxel from the images in (1); (3) Get the oxygen image by use of the quantitative relation between oxygen concentration value and T1 value.

Clearly, the key problem is to reconstruct the UESD images. So, we refer to UESD image as EPR image in the work.

For three dimensional (3D) pulsed EPRI, the data is regarded as the projection data. A one dimensional projection signal at a specific angle may be obtained by inverse Fourier transform of the EPR signal at that angle. All projection signals in the full angle range make up the 3D Radon transform of the imaged object [5]. Image reconstruction for 3D EPRI is, in essence, to reconstruct the object from its projections via 3D inverse Radon transform.

The traditional reconstruction algorithm for 3D EPRI is the 3D filtered backprojection (FBP) algorithm [5]. FBP needs angle-densely collected projections to achieve accurate images [10]. Similar to magnetic resonance imaging (MRI) [11], the main disadvantage of EPRI is too long scanning time for collecting enough projections. For example, to scan the complex physical phantom considered in the work needs about 11 minutes to collect 828 projections, using which high quality EPR image may be reconstructed by FBP algorithm. A projection at a specific angle is obtained by repeatedly collecting projections and then averaging them to suppress the random noise and achieve high signal-to-noise (SNR). So, though the relaxation time of EPRI is much shorter than that of MRI, the whole scanning time is still too long.

There are two ways to speed up the scanning process: one is sparse-view sampling and the other one is low-SNR sampling. Sparse-view sampling means just collecting projections at sparse views, for example just collecting 208 projections sparsely relative to collecting 828 projections densely. Low-SNR sampling means reducing the repeating times for collecting a projection signal at a specific angle. Sparse-view sampling leads to the insufficient of the projection views and low-SNR sampling leads to the decrease of SNR of the projections. If FBP algorithm is used for sparse-view sampling, the streak artifacts will be introduced in the reconstructed image [6]. If low-SNR projections are used in FBP, the reconstructed image will be too noisy [12].

Fortunately, the compressed sensing (CS) based image reconstruction methods are competent to accurate sparse reconstruction [13]. In CS-based algorithms, total variation (TV) minimization algorithms have been deeply investigated and well applied to various imaging modality for accurately reconstructing images from sparsely sampled data. For example, in computed tomography (CT), TV-minimization algorithm has been used in cone-beam CT [14], [15], C-arm CT [16], and short-scan CT [17] to perform sparse reconstruction. In EPRI, we have designed a data divergence constrained, TV minimization (DDcTM) model to reconstruct EPR images accurately from sparse-view projections [6].

In the work, we will investigate how to accurately reconstruct EPR images from fast-scanned, low-SNR projections. TV minimization may also achieve high accurate reconstructions from this type of noisy projection data. This is because

TV minimization is also a denoising method, which was used initially in image denoising in 1996 [18]. In TV minimization algorithm, the effect of TV norm is to select one image with the minimal TV value from the convex defined by data fidelity term. Clearly, TV based algorithm has denoising effect during the iterative reconstruction process, so it may be used in noisy data cases.

The task of this work is similar to accurately reconstructing images from noisy projection data in low-dose CT. Bian *et al.* applied TV algorithm to low-dose dedicated breast CT, finding the TV algorithm may accurately reconstruct the small contrast and fine structure of breast tissues which is too difficult for FBP algorithm to reconstruct accurately [12]. In image-guided radiation therapy, Han *et al.* [19] investigated TV algorithm on the on-board imager (OBI), focusing on low dose reconstruction, and their study results show that the reconstructions are with improvement, relative to clinical FDK reconstruction, in both visualization and quantitative assessments in terms of the devised utility metrics. Ding and Hu [20] combined TV minimization and sparse dictionary learning techniques, and achieved accurate reconstruction from noisy data in low-dose CT. It is also reported that adaptive statistical iterative reconstruction (ASIR), developed by GE company, may reconstruct high quality abdominal images from projections with lower (by 23–66%) radiation doses compared with FBP images reconstructed from routine-dose projection data [21].

Encouraged by these successful applications of the optimization-based models, especially TV models, in noisy-projection-type low-dose CT, in the work, we will investigate and evaluate the accurate-reconstruction ability of a TV based algorithm from noisy projection data obtained by low-SNR sampling pattern to speed up the scanning process.

In the previous optimization models used in low-dose CT, DDcTM models are often employed. DDcTM models use the TV norm as the objective function and use data divergence term as the constraint. In the work, we consider an opposite thought: use the TV norm as the constraint and data divergence term as the objective function. The optimization model is referred to as the TV constrained, data divergence minimization (TVCdM) model. In the model, the constraint parameter is the TV bound whose value is not so sensitive as the constraint parameter, data tolerance, in DDcTM, so its selection is relatively easier. The model has been successfully evaluated in short scan CT [17], C-arm CT [16] and positron emission tomography (PET) [22].

There exist many algorithms to solve convex optimization models, including adaptive steepest descent-projection onto convex sets (ASD-POCS), alternating direction method of multipliers (ADMM) [23] and split Bregman [24], etc. In the work, we will use a novel solving algorithm, Chambolle-Pock (CP) algorithm [25], [26]. CP algorithm is a first order primal dual algorithm framework. It may solve all the convex optimization models, no matter it is smooth or non-smooth. Meanwhile, it may solve not only unconstraint but also constraint optimization models. Its algorithm parameters

may be determined by fixed calculation equations. And the most attractively, all the sub-problems in the CP algorithm instances have close forms [26]. All the advantages above promote us to use it as the solver of TVcDM.

In the work, the EPR image is modeled to be the solution of TVcDM and the CP algorithm is tailored to solve the model. We validate the TVcDM-CP algorithm using 3D mathematical phantom and evaluate the characteristics of the algorithm using a complex physical phantom.

In Section II, we describe the EPRI imaging model, TVcDM model, CP algorithm and its implementation considerations. In Section III, we perform algorithm-verification study, following which, a complex physical phantom reconstruction is performed using low-SNR sampling pattern to evaluate the high accurate reconstruction ability of the algorithm from noisy projections in Section IV. Finally, a brief discussion on the TVcDM-CP algorithm for fast-scanned, noisy EPRI projections is given in Section V.

II. METHODS

In the section, we will describe the TVcDM-CP algorithm for EPRI according to the following sequence: imaging system modeling, optimization model designing, CP algorithm design, reconstruction parameters, convergence condition metrics and image quality metrics.

A. CONTINUOUS-TO-CONTINUOUS (CC)-DATA MODEL

As mentioned, the continuous-to-continuous (CC)-data model in pulsed EPRI can be characterized by the Radon transform. We discuss briefly the CC-data model based upon which the DD-data model is introduced for EPRI in Sec. II.B below.

As shown in Fig. 1, $p(t, \varphi, \theta)$, the 3D Radon transform of 3D object function $f(x, y, z)$, can be expressed as

$$p(t, \varphi, \theta) = \iiint_{\Omega} f(x, y, z) \delta(x \cos \varphi \sin \theta + y \sin \varphi \sin \theta + z \cos \theta - t) dx dy dz, \quad (1)$$

where $p(t, \varphi, \theta)$ represents the integration of 3D object function $f(x, y, z)$ over a plane, specified by $x \cos \varphi \sin \theta + y \sin \varphi \sin \theta + z \cos \theta = t$, with distance t to the origin of the coordinate system and a unit vector $(\cos \varphi \sin \theta, \sin \varphi \sin \theta, \cos \theta)$ perpendicular to the plane; θ is the angle between the z -axis and the unit vector, and φ is the angle between the x -axis and the component of the unit vector on the xy -plane; $\delta(\cdot)$ denotes the Dirac function; and $\Omega \in \mathbb{R}^3$. The FBP algorithm can be used for solving $f(x, y, z)$ from full knowledge of $p(t, \varphi, \theta)$ over angular ranges $\theta \in [0, \pi/2]$ and $\varphi \in [0, 2\pi]$ [5]. In other words, accurate FBP reconstruction of $f(x, y, z)$ requires a large number of measurements of $p(t, \varphi, \theta)$ densely sampled over the angular ranges.

B. DISCRETE-TO-DISCRETE (DD)-DATA MODEL

Unlike the 3D FBP algorithm that reconstructs images by solving the CC-data model in Eq. (1), the optimization-based

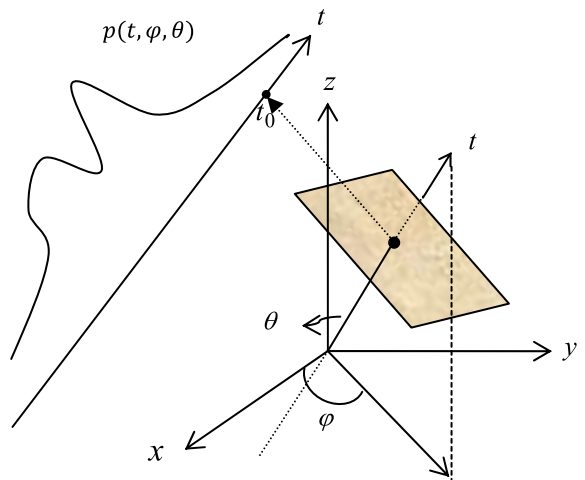


FIGURE 1. A schematic diagram of the 3D Radon transform. $p(t, \varphi, \theta)$ is 1D spatial projection at angle (φ, θ) . The shaded parallelogram denotes a plane $\cos \varphi \sin \theta + y \sin \varphi \sin \theta + z \cos \theta = t_0$. A measurement on the projection, $p(t_0, \varphi, \theta)$, is the surface integral of the 3D object on the plane represented by the parallelogram. For simplicity, the 3D object is not presented in the figure, and readers may imagine that the object is located at the 3D space, whose position is defined by the coordinate system. The support of the object is a sphere whose diameter is the length of the projection signal.

reconstruction is based on a DD-data model in which data and image are represented in discrete form. Specifically, a DD-data model can be derived from the CC-data model for EPRI as

$$\mathbf{g} = \mathbf{A}\mathbf{u}, \quad (2)$$

where vector \mathbf{g} of size $M = N_m N_a$ denotes the discrete model data, N_a the number of projection views, each of which is specified by a pair of discrete values of (φ, θ) , and N_m the number of measurements on each projection.

In (2), vector \mathbf{u} of size $N = N_x N_y N_z$ denotes a discrete image array. N_x , N_y , and N_z are numbers of voxels along the x -, y -, and z -axis, respectively.

System matrix \mathbf{A} of size MN in which entry $A_{m,n}$ represents the intersection area between the plane corresponding to the m^{th} measurement and the n^{th} voxel of the image. Clearly, the DD-data model can accommodate naturally the discrete nature of the data and image in real-world EPRI.

The sampling angle of a projection is determined by (φ, θ) with $\theta \in [0, \pi/2]$ and $\varphi \in [0, 2\pi]$. For uniformly distributing the sampling views, we use equal-solid angle sampling pattern [27]. The calculation steps of the angle set for equal solid angle are described below.

Step 1, Determine the number of θ , N_θ ,

Step 2, Calculate the θ values: $\theta_i = \frac{\pi}{2N_\theta} \left(i - \frac{1}{2} \right)$, $i = 1, 2, \dots, N_\theta$,

Step 3, Calculate the number of φ , N_φ for each θ : $N_\varphi(\theta_i) = \text{round}(2N_\theta \sin \theta_i)$,

Step 4, Calculate the φ values for each fixed θ : $\varphi_k(\theta_i) = \frac{2\pi}{N_\varphi(\theta_i)} \left(k - \frac{1}{2} \right)$, $k = 1, 2, \dots, N_\varphi$.

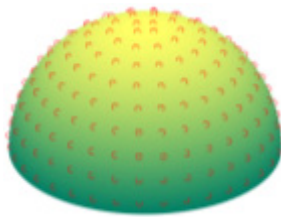


FIGURE 2. Schematic diagram of the equal solid angle pattern. Each small red circle indicates a specific sampling angle. Clearly, the distribution of the sampling angles are uniform.

Clearly, by fixing N_θ , we may get $N_a = \sum_{i=1}^{N_\theta} N_\varphi(\theta_i)$. For example, $N_\theta = 9$, then $N_a = 208$ projections uniformly distributed in the angle range may be denoted by Fig. 2.

The task of image reconstruction is to determine image vector \mathbf{u} from knowledge of model-data vector \mathbf{g} through inverting the DD-data model. Due to the size of matrix A and its ill-conditionness in practical EPRI, it is impossible that image reconstruction can be obtained through direct inversion of matrix A . Instead, as described below, we perform optimization-based image reconstruction by using knowledge of model-data vector \mathbf{g} and the DD-data model.

C. OPTIMIZATION MODEL

In the optimization-based reconstruction, we consider an TVcDM model [17], [22], [28], which is given by

$$\mathbf{u}^* = \arg \min_{\mathbf{u}} \|\mathbf{g}_m - \mathbf{A}\mathbf{u}\|_2^2 \quad \text{s.t. } \|\mathbf{u}\|_{\text{TV}} \leq t_1 \quad (3)$$

where \mathbf{u}^* denotes image of size N reconstructed, \mathbf{g}_m measured data vector of size M , $\|\mathbf{g}_m - \mathbf{A}\mathbf{u}\|_2^2$ the square of the ℓ_2 -norm of difference between measured data \mathbf{g}_m and model data \mathbf{g} , $\|\mathbf{u}\|_{\text{TV}}$ image-TV and t_1 the image-TV bound.

$\|\mathbf{u}\|_{\text{TV}}$ is the ℓ_1 -norm of the gradient magnitude image (GMI) $|D\mathbf{u}|_{\text{mag}}$:

$$\|\mathbf{u}\|_{\text{TV}} = \| |D\mathbf{u}|_{\text{mag}} \|_1 \quad (4)$$

where, $D = \begin{pmatrix} D_x \\ D_y \\ D_z \end{pmatrix}$ of size $3N \times N$, contains matrices D_x , D_y , and D_z of size $N \times N$ denoting discrete gradient transforms (DGT) along the x , y , and z axes, respectively.

The explicit forms of gradient transform D_x , D_y , and D_z are given by

$$(D_x f)_{i_x, i_y, i_z} = \begin{cases} f_{i_x, i_y, i_z} - f_{i_x-1, i_y, i_z} & \in [2, N_x] \\ 0 & i_x = 1, \end{cases} \quad (5)$$

$$(D_y f)_{i_x, i_y, i_z} = \begin{cases} f_{i_x, i_y, i_z} - f_{i_x, i_y-1, i_z} & \in [2, N_y] \\ 0 & i_y = 1, \end{cases} \quad (6)$$

$$(D_z f)_{i_x, i_y, i_z} = \begin{cases} f_{i_x, i_y, i_z} - f_{i_x, i_y, i_z-1} & \in [2, N_z] \\ 0 & i_z = 1 \end{cases} \quad (7)$$

where f is the discrete 3D object of size $[N_x, N_y, N_z]$ and i_x , i_y and i_z are the index along the x , y , and z axes, respectively.

When f is formed by concatenating its 3D array form into vector, it becomes \mathbf{u} , the image in (3). According to the relation of f and \mathbf{u} , matrices D_x , D_y , and D_z may be constructed by using (5), (6), and (7), respectively.

Thus, $D\mathbf{u}$ is a vector of size $3N$, denoting the DGT of the image. $|D\mathbf{u}|_{\text{mag}}$ is a vector of size N , denoting the GMI corresponding to the image \mathbf{u} . $\|\cdot\|_{\text{mag}}$ computes the magnitude of the 3D gradient vector at each voxel. The isotropic GMT uses ℓ_2 -norm for computing $\|\cdot\|_{\text{mag}}$ whereas the anisotropic GMT uses ℓ_1 -norm.

The isotropic GMT of image \mathbf{u} is used in the work and then we get

$$\|\mathbf{u}\|_{\text{TV}} = \sum_{n=1}^N \|(D_x \mathbf{u})_n (D_y \mathbf{u})_n (D_z \mathbf{u})_n\|_2 \quad (8)$$

D. THE CP ALGORITHM

Image reconstruction can be accomplished by solving the TVcDM model specified completely above. Considering the fact that the TVcDM model is convex and non-smooth, we use the CP primal-dual algorithm to solve the model, because the CP algorithm may solve any convex optimization model no matter smooth or non-smooth and because it has been demonstrated to possess this capability for robust reconstructions of CT and PET images [17], [22]. In this work, we tailor the CP algorithm to solve the convex, non-smooth model in (3) and reconstruct images from 3D EPRI data, especially from noisy-projection data.

We consider a new optimization model that is obtained by incorporating two parameters into the TVcDM model in (3)

$$\mathbf{u}^* = \operatorname{argmin}_{\mathbf{u}} \frac{\lambda}{2} \|\mathbf{g}_m - \mathbf{A}\mathbf{u}\|_2^2 \quad \text{s.t. } \nu \|\mathbf{u}\|_{\text{TV}} \leq \nu t_1 \quad (9)$$

It can readily be observed that the optimization models in (3) and (9) specify identical solutions. Therefore, we consider the CP algorithm for solving (9) to achieve the reconstruction specified by (3). As shown previously [16], [17], [28], the CP algorithm tailored to solve (9) includes parameters λ and ν , which can in turn be tuned to increase the algorithm's convergence rate. It is worth noting that, while parameters λ and ν can affect the convergence path/rate of the tailored CP algorithm [16], they have no impact on the solution specified by (3).

We show in Table 1 the pseudo-codes of the tailored CP algorithm for solving the model in (9) [16], [17], [28]. In Table 1, $\|\cdot\|_{\text{sv}}$ denotes the largest singular value of a matrix, which can be calculated by use of Algorithm 8 in [26]; vectors \mathbf{u} , $\bar{\mathbf{u}}$, and \mathbf{s} are with size N , vector \mathbf{p} is with size M , and vectors \mathbf{q} and \mathbf{a} are of size $3N$; vector $\mathbf{1}_I$ in line 6.3 is a vector of size N with all entry set to 1; and \mathbf{u}_{conv} represents the converged reconstruction satisfying the practical convergence conditions described in each of the studies below. In line 6.2, projection operation **ProjectOnto** ℓ_1 **Ball** $_{\nu t_1}$ can be computed by use of the pseudo-codes shown in Table 2 below.

In Table 2, \mathbf{x} denotes a vector of size N , a the radius of the ℓ_1 ball, \mathbf{m} a vector of size N with its i th entry $m_i = |x_i|$,

TABLE 1. Pseudo-codes of the CP algorithm for solving (9).

INPUT: $\mathbf{g}_m, \mathbf{A}, \lambda, b$, and t_1
1: compute $v_A = \frac{\ \mathbf{A}\ _{SV}}{\ \mathbf{D}\ _{SV}}$, $v = b v_A$, and $L = \left\ \begin{matrix} \mathbf{A} \\ v_D \end{matrix} \right\ _{SV}$
2: $\sigma = \frac{1}{L}$; $\tau = \frac{1}{L}$; $\theta = 1$; $n = 0$
3: $\mathbf{u}_0 = 0$; $\bar{\mathbf{u}}_0 = 0$; $\mathbf{p}_0 = 0$; $\mathbf{q}_0 = 0$
4: repeat
5: $\mathbf{p}_{n+1} = (\mathbf{p}_n + \sigma(\mathbf{A}\bar{\mathbf{u}}_n - \mathbf{g}_m))/(1 + \sigma/\lambda)$
6: 6.1 $\mathbf{a} = \mathbf{q}_n + \sigma v D \bar{\mathbf{u}}_n$
6: 6.2 $\mathbf{s} = \text{ProjectOnto}\ell_1\text{Ball}_{vt_1}(\mathbf{a} _{\text{mag}}/\sigma)$
6: 6.3 $\mathbf{q}_{n+1} = \mathbf{a}(\mathbf{1}_I - \sigma s / \mathbf{a} _{\text{mag}})$
7: $\mathbf{u}_{n+1} = \mathbf{u}_n - \tau(\mathbf{A}^T \mathbf{p}_{n+1} + v \mathbf{D}^T \mathbf{q}_{n+1})$
8: $\bar{\mathbf{u}}_{n+1} = \mathbf{u}_{n+1} + \theta(\mathbf{u}_{n+1} - \mathbf{u}_n)$
9: $n = n + 1$
10: until the practical convergence conditions are satisfied
OUTPUT: image \mathbf{u}_{conv}

TABLE 2. Pseudo-codes for ProjectOnto ℓ_1 Ball $_a$ operation [28].

1: FunctionProjectOnto ℓ_1 Ball $_a(x)$
2: if $\ \mathbf{x}\ _1 \leq a$ then
3: return \mathbf{x}
4: end if
5: $\mathbf{m} = \mathbf{x} $
6: Sort \mathbf{m} in descending order
7: $k = \max(j)$ such that $m_j - \frac{1}{j}(\sum_{i=1}^j m_i - a) > 0$ for all $j \in [1, N]$
8: $\theta = (1/k)(\sum_{i=1}^k m_i - a)$
9: $\mathbf{w} = \max(\mathbf{x} - \theta, 0)$
10: return $\mathbf{w} \cdot \text{sign}(\mathbf{x})$
11: end function

$\text{sign}(\mathbf{x})$ a sign function defined as $\text{sign}(x_i)$ equals -1 for $x_i < 0$, 0 for $x_i = 0$, and 1 for $x_i > 0$.

E. RECONSTRUCTION PARAMETERS

We divide the reconstruction parameters into two types: model parameters and algorithm parameters.

Model parameters are the parameters in (3), which decide the designed solution to the optimization model. Algorithm parameters are the parameters related to the CP algorithm, which may impact the convergence rate/path.

The model parameters used for specifying the optimization model in (9) include system matrix \mathbf{A} , gradient transform matrix \mathbf{D} , image basis (e.g., image voxel), and TV bound t_1 . Clearly, the solutions of the optimization model depend on the selection of model parameters. In this work, we use isotropic cubic voxels as image basis and calculate gradient matrix \mathbf{D} on-the-fly following (5)-(7). Matrix \mathbf{A} corresponds to the forward projections that can be computed on-the-fly by use of the voxel-driven projection model [29]. The selection of TV bound will be discussed in complex physical phantom study below.

Algorithm parameters λ, v, σ, τ , and θ are involved in the CP algorithm, as described in the pseudo-codes in Table 1. In particular, parameters σ, τ , and θ are calculated in line 2 of Table 1, whereas parameters λ and v have no impact on the solution to the optimization model but can affect the algorithm convergence rate, which will be investigated in the algorithm-verification study below.

F. METRICS FOR CONVERGENCE CONDITIONS

The CP algorithm can mathematically converge to the solution to the optimization model when the iteration number approaches infinity. However, it is practically impossible to achieve the mathematical convergence due to the finite computer precision and practical iteration time. Therefore, it is necessary to design practical convergence conditions to which the CP algorithm can practically achieve for reconstructions of the mathematical phantom and physical phantom.

The metrics for mathematical phantom reconstructions are NDE (Normalized Data Error), NOE (Normalized Object Error) and NTVE (Normalized TV Error), defined by

$$\text{NDE}(\mathbf{u}_n) = \|\mathbf{g}_m - \mathbf{A}\mathbf{u}_n\|_2 / \|\mathbf{g}_m\|_2 \quad (10)$$

$$\text{NOE}(\mathbf{u}_n) = \|\mathbf{u}_n - \mathbf{u}_{\text{truth}}\|_2 / \|\mathbf{u}_{\text{truth}}\|_2 \quad (11)$$

$$\text{NTVE}(\mathbf{u}_n) = |(\|\mathbf{u}_n\|_{\text{TV}} - t_1)| / t_1, \quad (12)$$

where $\mathbf{u}_{\text{truth}}$ is the known mathematical phantom image. NDE evaluates the distance between the model data at iteration n and the measured data; NOE evaluate the distance between the reconstructed object at iteration n and the truth image; and NTVE is the relative error of the TV value compared to TV bound, t_1 .

For physical phantom reconstruction, there is not a truth image, so there are only two metrics for evaluating the convergence status. One is NTVE and the other one is the dNDE (differential Normalized Data Error), defined as

$$\text{dNDE}(\mathbf{u}_n) = |\text{NDE}(\mathbf{u}_n) - \text{NDE}(\mathbf{u}_{n-1})| \quad (13)$$

In real data reconstructions, noise and system inconsistency always exist, so NDE cannot reach 0 even if the iteration index n approaches infinity. When the iteration process enters the stable status, NDE should converge to a positive number, which is unknown. Thus, we may use dNDE to evaluate the change of NDE between two iterations. A small enough dNDE means practical convergence.

G. METRICS FOR IMAGE QUALITY EVALUATION

For simulation reconstruction, we just use NOE(\mathbf{u}_{conv}) to evaluate the reconstruction accuracy, i.e. image quality, for the existence of truth image.

For real data reconstruction, we use two metrics to evaluate the image quality. One is rNOE (reference-image-based NOE) and the other one is CNR (Contrast-Noise-Ratio) [14], which are defined as

$$\text{rNOE}(\mathbf{u}_{\text{conv}}) = \|\mathbf{u}_{\text{conv}} - \mathbf{u}_{\text{ref}}\|_2 / \|\mathbf{u}_{\text{ref}}\|_2 \quad (14)$$

and

$$\text{CNR}(\mathbf{u}_{\text{conv}}) = \frac{2|m_s - m_b|}{\delta_s + \delta_b}, \quad (15)$$

where m_s and m_b are the mean values of the signal-ROI-image s and background-ROI-image b in the convergent image, respectively; and δ_s and δ_b are the standard deviations

of image values within the ROIs s and b , respectively.

$$m_w = \frac{1}{N} \sum_{i=1}^N w_i \quad (16)$$

$$\delta_w = \sqrt{\frac{1}{N-1} \sum_{i=1}^N (w_i - m_w)^2}, \quad (17)$$

where w_i denotes the i th entry of ROI-image w .

In real data reconstruction, for the truth image does not exist, one may just use a high quality image as a benchmark to be reference image, \mathbf{u}_{ref} . CNR may be used to evaluate the ability to reconstruct low-contrast structure. In the work, the complex physical phantom includes a bottle filled with low density spin probe, i.e it is a low-contrast object, so we use CNR to evaluate its reconstruction quality.

III. ALGORITHM-VERIFICATION STUDY

To verify the correctness of the imaging system modeling, optimization model designing, CP algorithm derivation and its computer implementation, a simulation study is necessary. In the work, we use a mathematical phantom to perform the study, focusing on the convergence behavior. Additionally, the impact of the algorithm parameters, λ and ν , on convergence rate is also studied.

A. ALGORITHM VERIFICATION

To verify the correctness of an algorithm, one may use a mathematical phantom to generate ideal and sufficient data and then reconstruct the object. If the algorithm and its computer implementation are both correct, the reconstructed object should achieve a very high accuracy under the confine of computer float number precision.

In the study, we consider a 3D mathematical phantom of sphere-shape embedded with 5 spherical inserts. The phantom image is of size $N = 40 \times 40 \times 40$, whose middle transverse slice is shown in Fig. 3(a). Using system matrix A described above, we generate projection data of size $M = N_m N_a$ with $N_m = 40$, $N_a = 1,596$, respectively, from the numerical phantom. The 1,596 projections are uniformly distributed over a hemisphere, i.e. we use equal solid angel sampling pattern [30]. The size of the voxel and the sampling interval on the projection are both set to 1.

For the imaging model, i.e. the system of linear equations shown in (2), there are $N = 40 \times 40 \times 40 = 64,000$ unknown numbers and $M = 40 \times 1,596 = 63,840$ equations. The linear system is completely consistent and has sufficient effective equations, so using the TVcDM optimization model may achieve high accuracy.

We calculate the TV of the truth image and use it as model parameter t_1 and set $\lambda = 1$ and $\nu = \nu_A$ to achieve fast convergence. σ , τ and θ are set up by its determination method shown in Table 1. The practical convergence conditions are

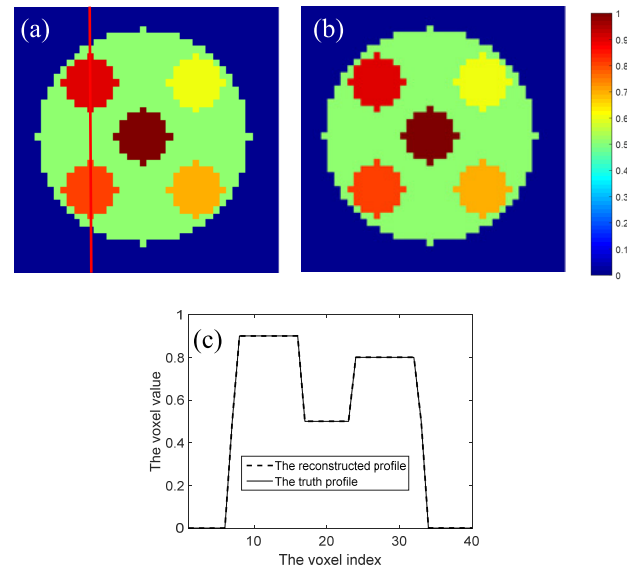


FIGURE 3. The middle transverse slice image of the 3D mathematical phantom (a), the corresponding reconstructed image (b) and the profile-comparison (c). In (c), the profile curves are along the red line shown in (a). The display window of (a) and (b) is [0, 1].

designed as

$$\text{NDE}(\mathbf{u}_n) \leq 10^{-3} \quad (18)$$

$$\text{NOE}(\mathbf{u}_n) \leq 10^{-4} \quad (19)$$

$$\text{NTVE}(\mathbf{u}_n) \leq 10^{-3} \quad (20)$$

Under the imaging conditions, using the model parameters and algorithm parameters determined above and controlled by the practical convergence conditions designed above, we implement the TVcDM-CP algorithm and show the reconstructed image in Fig. 3 (b). For further visual inspection, the reconstructed profile and the truth profile are shown in Fig. 3 (c). Fig. 4 shows the convergence curves of the three convergence-condition metrics.

The iteration stops at iteration **6051**. At the iteration point, the practical convergence conditions are reached: NOE is less than 10^{-4} , NDE tends to 10^{-5} and NTVE is less than 10^{-3} . From the reconstructed image shown in Fig. 3 (b), one cannot distinguish any difference from the truth image shown in Fig. 3 (a). Further, we observe the reconstructed profile curve and the truth curve in Fig. 3 (c) and find they almost completely overlap. These qualitative and quantitative analysis shows that TVcDM-CP algorithm achieves high accurate reconstruction using ideal and sufficient projection data, validating that the components in the reconstruction chain from imaging system model to the final computer implementation are all correct.

From Fig. 4, we may observe the convergence behavior of the three metrics. Generally speaking, NOE, NDE and NTVE all have global descent trend. However, the iteration curve is not smooth. Especially, we see the NTVE gets a comparatively big vibration when its value has been small enough, for example less than 10^{-3} . During its vibration, NOE and NDE may continue to go down, indicating to move continually

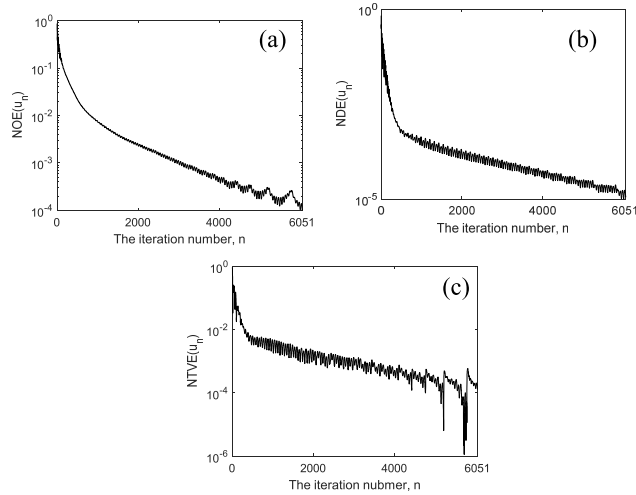


FIGURE 4. Plots of NOE (u_n), (a) NDE (u_n), (b) and NTVE (u_n) (c) as functions of iteration number in the algorithm verification study.

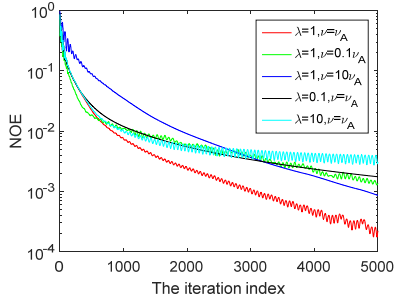


FIGURE 5. Convergence rate comparison of different selections of algorithm parameters λ and ν .

towards the truth image. Clearly, though the characteristics of descent with vibration exist, the CP algorithm may always achieve convergence and leads to the designed solution.

B. THE IMPACT OF THE ALGORITHM PARAMETERS, λ AND ν ON CONVERGENCE RATE

In III. A, we use $\lambda = 1$ and $\nu = \nu_A$ to achieve faster convergence rate. The two parameters are introduced to balance the magnitudes of the two convex functions corresponding to data divergence term and TV term. If better balance is obtained, faster convergence rate may be achieved.

We repeat the mathematical phantom reconstructions and stop at iteration 5,000 with the same reconstruction parameters except for the different selection of λ and ν to evaluate their impact on convergence rate.

From Fig. 5, we see that the convergence rate of the five different parameter pairs are different. $\lambda = 1$ and $\nu = \nu_A$ are the fastest pair, whereas $\lambda = 10$ and $\nu = \nu_A$ is the slowest one. It seems to suggest that λ should not be too big. However, There is not a certainly law on how the two parameters impact the convergence rate. Instead, one may run reconstructions with different parameter pairs and select the fastest one to perform further reconstructions for their determination is imaging conditions dependent.

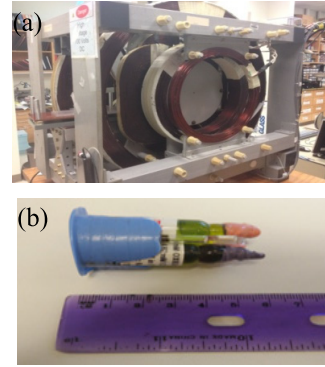


FIGURE 6. A prototype EPR imager (a) and a complex physical phantom consisting of 3 bottles and 3 tubes (b).

IV. REAL DATA RECONSTRUCTION

After the algorithm-verification study, we perform real data reconstructions using a complex physical phantom scanned by EPR imager to evaluate if TVcDM-CP algorithm may reconstruct EPR image more accurate than FBP algorithm from fast-scanned, noisy projection data. Also, we will evaluate what is the limitation of low SNR, i.e. how much we may speed up the scanning process.

A. EPR IMAGER AND THE COMPLEX PHYSICAL PHANTOM

In the study, we collected data from a complex physical phantom by using a 250-MHz-pulse EPRI scanner (shown in Fig. 6(a)), controlled by SpecMan4EPR v2.1 [31], which was developed for EPR imaging *in vivo* physiology at The University of Chicago [9]. The complex physical phantom consists of three bottles and three tubes shown in Fig. 6 (b), and each bottle/tube is filled with solution with different levels of spin probe concentration.

B. PROJECTION DATA ACQUISITION AND FAST SCAN STRATEGY

In the study, we collect 828 projections distributed uniformly in the angle range. At each angle, the spatial projection signal is obtained by inverse FFT of the EPR signal. Other than MRI, the EPR signal is too noisy to be used in reconstruction of utility. The best denoising method is to collect the EPR signal repeatedly and average them for the noise is random and may hardly be removed acceptably by use of any existing denoising algorithm. Usually, we repeat 1,000 times and average the collected EPR signals to get one EPR signal at a specific angle. Too many repeating times introduce long scanning time. In the study, collecting 828 projections needs about 11 minutes, referred to as the *full* time.

If the repeating times are reduced, the whole scanning process may be speeded up. Correspondingly, the fast-scanned projection may be noisier for light average denoising. TVcDM-CP algorithm has ability to achieve more accurate EPR image than FBP for the use of optimization technique. To evaluate the accurate reconstruction of TVcDM-CP algorithm, we collect 1/8, 1/4, 1/2 and 1 full

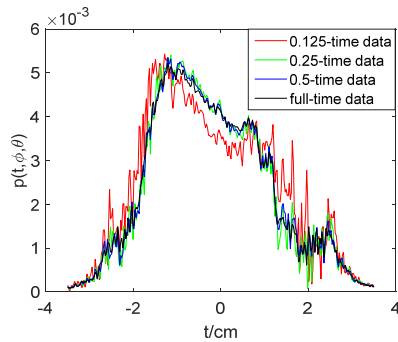


FIGURE 7. The projections at a specific angle within the four projection data sets. The length of the projection is 7cm.

time data to perform comparison study. Firstly, eight projection data sets collected respectively by use of 1/8 full time, i.e. 1.375 minutes are sampled. Then 1/4, 1/2 and 1 full time data may be obtained by averaging the first two, the first four and all the 1/8 full time data, respectively. For simplicity, we refer to the four projection data with different scanning time as 0.125-time data, 0.25-time data, 0.5-time data and full-time data.

In Fig. 7, the projections at a specific angle within the four projection data sets are plotted. From Fig. 7, it may be seen that the projection in the full-time data set has lower noise than the others and that the projection in the 0.125-time data set has the highest noise.

C. IMAGING CONDITIONS

The complex physical phantom was scanned by the 250MHz EPR imager. The length of the projection is 7cm. The sampling interval of the projection signal is 0.0875cm, so there are $N_m = 80$ measurements on each projection. The number of projections is $N_a = 828$. So, there are $M = N_m N_a = 80 \times 828 = 66,240$ measurements.

We reconstruct images of size $N = 80 \times 80 \times 80 = 512,000$ with voxels of size $0.0875\text{cm} \times 0.0875\text{cm} \times 0.0875\text{cm}$. Accordingly, the size of the system matrix A is $66,240 \times 512,000$. Its values may be calculated by accurate voxel-driven method [29].

D. RECONSTRUCTION PARAMETERS

We set $\lambda = 1$ and $\nu = \nu_A$ to achieve fast convergence. σ , τ and θ are set up by its determination method shown in Table 1. The practical convergence conditions are designed as

$$\text{dNDE}(\mathbf{u}_n) \leq 10^{-3} \quad (21)$$

$$\text{NTVE}(\mathbf{u}_n) \leq 10^{-3} \quad (22)$$

For the determination of TV bound t_1 , we reconstructed images from the full-time data set with multiple, different values of t_1 . Based upon visual inspection of these reconstructions, we select the value of t_1 that yields the reconstruction with highest resolution and least background noise. We show in Fig. 8 images within the $y = 44$ slice reconstructed with

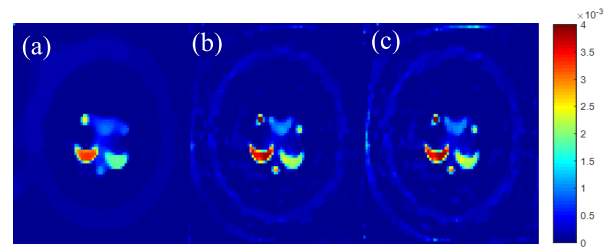


FIGURE 8. The $y = 44$ slice images of the reconstructed complex physical phantom with $t_1 = 0.1t_0$ (a), $0.2t_0$ (b), and $0.3t_0$ (c). The display window is $[0, 0.004]$.

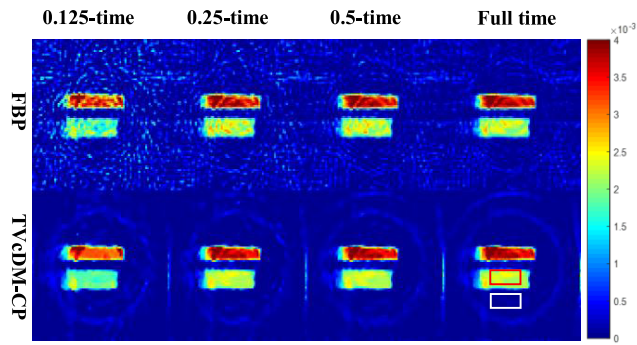


FIGURE 9. The $x = 31$ slice images of the reconstructed complex phantom. The text above the images indicates the projection type with different scanning time and SNR. The text on the left of the images indicates the used reconstruction algorithm, FBP and TVcDM-CP. The display window is $[0, 0.004]$. The red rectangle shown in image at Row 2 and Column 4 indicates the signal region whereas the white one indicates the background region for the calculation of the CNR of the reconstructed objects.

$t_1 = 0.1t_0, 0.2t_0$, and $0.3t_0$, respectively, where t_0 is the TV value of the FBP reconstruction from the full-time data.

It can be observed that the reconstruction with $t_1 = 0.1t_0$ has considerably blurry boundaries and that the reconstruction with $t_1 = 0.3$ possesses severe artifacts/noise in the background. Conversely, the reconstruction with $t_1 = 0.2t_0$ appears to yield both sharp boundaries and suppressed background noise simultaneously. Therefore, we select $t_1 = 0.2t_0$ for image reconstruction of the complex physical phantom.

E. THE RECONSTRUCTIONS OF THE COMPLEX PHYSICAL PHANTOM

According to the reconstruction parameters determination method shown in IV. D and the imaging conditions shown in IV. C, we reconstruct EPR images using the TVcDM-CP algorithm from 0.125-time data, 0.25-time data, 0.5-time data and full-time data.

We use visual inspection and quantitative analysis to evaluate the reconstruction quality. Figs 9, 10 and 11 show the $x = 31$, $y = 48$ and $z = 48$ slice images of the complex physical phantom, respectively. Figs 12 and 13 show the rNOE and CNR of the reconstructed objects, respectively.

For the different projection data set collected in different scanning time, their SNRs are different. Full time data has the highest SNR whereas the 0.125-time data has the lowest SNR.

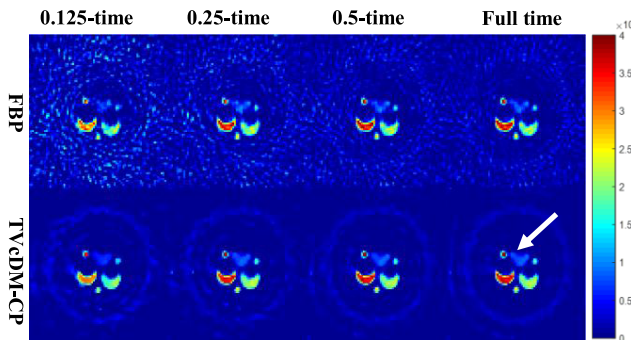


FIGURE 10. The $y = 48$ slice images of the reconstructed complex phantom. The meaning of the text and display window are the same with those in Fig. 9. The white arrow points to the low-density bottle.

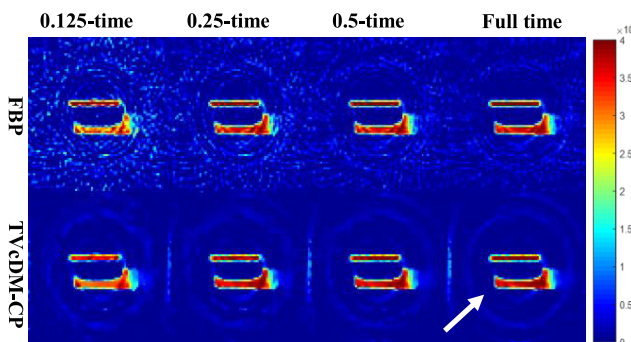


FIGURE 11. The $z = 48$ slice images of the reconstructed complex phantom. The meaning of the text and display window are the same with those in Fig. 9. The white arrow points to the high density bottle.

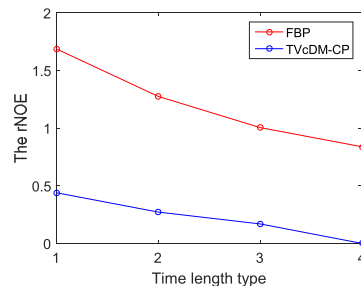


FIGURE 12. The rNOE of the reconstructed complex physical phantom by use of FBP and TVcDM-CP algorithms. The time length types 1, 2, 3 and 4 indicate 0.125-, 0.25-, 0.5- and the full time data, respectively.

From Figs 9, 10 and 11, we may notice that the TVcDM-CP (For simplicity, we refer to TVcDM-CP as CP hereafter) images has lower noise than FBP images if the same data used. With the decrease of the scanning time, the noise in FBP images becomes higher and higher. However, the change of noise level with the decrease of the scanning time for CP images is not so sensitive. This is because the TV norm in the CP algorithm may also reduce the noise except for its main function of suppressing streak artifacts introduced by sparse-view projections. Even that CP image reconstructed from 0.125-time data has lower noise than FBP image reconstructed from full time data.

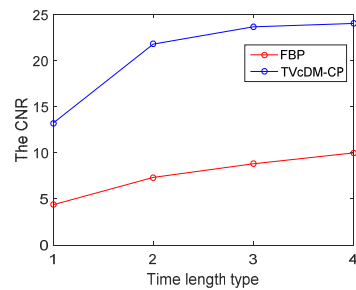


FIGURE 13. The CNR of the reconstructed complex physical phantom by use of FBP and TVcDM-CP algorithms. The time length types 1, 2, 3 and 4 indicate 0.125-, 0.25-, 0.5- and the full time data, respectively. The signal and background ROIs are indicated in row 2 and column 4 in Fig. 9.

We refer to the bottle filled with high concentration spin probes as the high density bottle. In the pseudocolor images shown in Figs 9, 10 and 11, the blue color indicates low concentration whereas the red color indicates high concentration. So, the high density bottle is red.

In Fig. 11, a white arrow points to the high density bottle. The solution in the bottle has uniform spin probe distribution, so the image of the high density bottle should be color-uniform. Observing all the high density bottles in Fig. 11 carefully, we find that the CP bottle-images are more uniform than the FBP bottle-images, which suffer from vibration artifacts, if the same projection data used, indicating that CP has ability to suppress vibration artifacts coming from low SNR projection data. With the decrease of the scanning time, FBP bottle-image shows more and more serious vibration artifacts. However, the change of CP bottle-image is not so sensitive. Even that CP bottle-image reconstructed from 0.25-time data is more uniform than FBP bottle-image reconstructed from full time data.

We refer to the bottle filled with low concentration spin probes as the low density bottle. For image reconstruction, low contrast object reconstruction is a challenging task. In the complex physical phantom, the reconstruction of the low density bottle is challenging for it is a low contrast object compared to the zero-background and the SNR of the projection signal is low.

In Fig. 10, the low density bottle is pointed by the white arrow. Observing all the low density bottles in Fig. 10 carefully, we may observe that the CP bottle-images have clear and uniform selenodont structure. However, the FBP bottle-images in the first row of Fig. 10 all have been distorted because of the noise in the projections. The FBP bottle-image reconstructed from 0.125-time data cannot even be distinguished from the whole slice image for the bottle-selenodont shape has been seriously distorted and its color is very similar to the color of the background noise. With the decrease of the scanning time, the FBP bottle-images become more and more distorted. However, the CP bottle-images is not so sensitive to the decrease of the scanning time. Even that the CP bottle-image reconstructed from 0.25-time data has clearer structure than FBP bottle-image reconstructed from full time data.

Besides the analysis based on visual inspection above, we also perform quantitative analysis based on the rNOE and CNR as function of time length type.

From Fig. 12, it may be seen that the reconstruction error evaluated by metric rNOE of CP is lower than that of FBP. This shows that CP algorithm has ability of accurately reconstructing object from noisy data, from which FBP algorithm always leads to noisy images. The error of CP algorithm using 0.125-time data is even lower than that of FBP using full time data.

From Fig. 13, it may be seen that the CNR of CP is always higher than that of FBP no matter which type of projection data is used. This shows that CP may accurately reconstruct low-contrast image compared with FBP. The CNR of CP using 0.125-time data is even higher than that of FBP using full time data.

By visual inspection and quantitative analysis of the reconstructed images by CP and FBP, It may be concluded conservatively that CP algorithm using 0.25-time data may outperforms FBP algorithm using full time data. Thus, the whole scanning time may be reduced to one fourth of the full time, i.e. four times acceleration factor for scanning process can be achieved by use of the CP algorithm.

V. DISCUSSION AND CONCLUSIONS

To speed up the scanning process of EPR imaging, we reduce the repeating times for obtaining a projection signal at each view angle. Reducing repeating times will certainly introduce higher random noise in the projection data. Thus, the images reconstructed by the traditional FBP algorithm from these fast-scanned, noisy projections are always too noisy to be used for further image post-processing.

In the work, we use algorithm-enabled technique to improve the reconstruction quality from noisy projections. We model the EPR image as the solution of a TVcDM model, in which the data divergence is minimized subject to a constraint on the image TV. To solve the TVcDM model, we design the corresponding CP algorithm instance according to the CP algorithm framework.

We have performed studies to verify the correctness of the CP algorithm and its computer implementation via a mathematical phantom and characterize the performance of the CP algorithm via a complex physical phantom. The visual inspection and quantitative analysis both demonstrate that CP algorithm may achieve more accurate EPR images from projections collected within a factorial scanning time than FBP algorithm. With the decrease of the scanning time, equivalently the reduction of the SNR of the projection data, the FBP algorithm introduces higher and higher noise and more and more serious distortion-artifacts. However, the CP algorithm may effectively suppress the noise and artifacts, achieving higher imaging quality. To be conservative, the CP reconstruction from one fourth full time data outperforms the FBP reconstruction from full time data. Thus, we may achieve at least four times of acceleration of the scanning process.

It seems that the CP images reconstructed from 0.125-time data is also more accurate than FBP images reconstructed from full time data according to the quantitative analysis of rNOE and CNR shown in Figs 12 and 13. However, observing the CP slice-images reconstructed from 0.125-time data and 0.25-time data in Figs 9, 10 and 11, we may find that the bottle-images or tube-images reconstructed from 0.125-time data always have lighter color compared to those images reconstructed from 0.25-time data, indicating smaller voxel values. To be objective, we may not claim that CP reconstruction from 0.125-time data is acceptable.

Like all the optimization-based image reconstruction algorithms, the reconstruction parameters, including model parameters and algorithm parameters, are very critical to reconstruction quality or convergence rate. In the work, during the algorithm-verification study and real data study, we have investigated these parameters deeply. Model parameters determine the solutions of the optimization model, i.e. the reconstructed images. Algorithm parameters, referred to as the parameters in the CP solving algorithm, do not determine the solution of the optimization model, but may impact the convergence rate and path. Different TV bound may lead to different solution: too large value introduces higher noise whereas too small value leads to smoother reconstructed images. According to the insight on TV bound, we may select the optimal value to achieve high quality reconstructions. The introduced algorithm parameters, λ and ν , may impact the convergence rate. We may select the best pair by running the reconstruction algorithm with diverse pairs of λ and ν to achieve the fastest convergence rate.

In the work, the data divergence term is of ℓ_2 -norm form. It may be also of theoretical interest and practical significance to investigate new TVcDM model with data divergence term of ℓ_1 -norm form or Kullback-Leibler (KL)-divergence form. The different forms of data divergence term are suitable for different noise types. However, the noise type of EPR projection signal is not typical and clear, so it is necessary to characterize the performance of TVcDM model with different data divergence forms.

TV algorithm is a popular optimization-based algorithm and has solid theoretical basis. In 1992, Rudin *et al.* [32] proposed the famous ROF model according to variational theory and found that TV algorithm may suppress noise and preserve edge simultaneously. In 2006, Donoho [33] proposed the compressed sensing (CS) theory and used TV algorithm as a classical CS-based algorithm to demonstrate the theory. Additionally, TV may also be regarded as a new regularization technique. Thus, TV algorithm has at least three theory basis, the variational theory, the CS theory and the regularization theory.

In image restoration area, some studies have pointed out that the TV minimization may lead to staircase or blocky artifacts [34] and many variational TV model, for example high-order TV model [35], have been proposed to suppress the staircase effect. However, though the staircase artifact may be observed if the image has smooth transition region in image

restoration, we must point out that the artifact is very weeny in image reconstruction. In 2006, when Sidky *et al.* proposed the TV minimization based image reconstruction algorithm for CT, they had noted the potential and possible disadvantage of TV model and performed reconstruction from a Shepp-Logan phantom of wavy background. But they found that the reconstructed images and its center-line profiles have *not* blocky or staircase artifacts [13]. We may give a qualitative explanation. In image denoising, the data fidelity constraint is very loose, so the staircase is easy to come out if the image has transition region. However, in image reconstruction, the data fidelity term is the data divergence between the measured projection data and the guessed data. The data and the image are connected by the forward imaging process. The measured projection signal has not staircase feature, so if the inter-iteration image has staircase artifacts after the TV regularization step, the artifacts will vanish after the data fidelity step to respect the projection data. In fact, during our reconstruction practice in EPR imaging, we never saw the staircase effect. Another possible reason may be that the EPR image is functional image rather than structure image and has not subtle transition region and has more piecewise-constant regions that is very suitable for TV models.

This is why we have focused on TV models several years in EPR imaging though some potential alternative optimization-based algorithms, for example non-local TV [36], dictionary learning algorithms [37], have been proposed.

Recently, the deep-learning based image reconstruction methods have attracted our attentions [38]–[41]. It is possible that the regularization term or the whole reconstruction process may be learned by training the deep network. After the open of the EPRI data by the NIH center for EPR imaging, we are interested in investigating the application of deep-learning based reconstruction methods.

Though we have successfully investigated the TVcDM-CP algorithm using real scanned data of a challenging complex physical phantom, it is more important and challenging to evaluate the reconstruction performance using pre-clinical data of mouse-tumor.

Currently, we are investigating different designs of TVcDM model and characterize their performance and beginning to apply the TVcDM-CP algorithm to pre-clinical *in vivo* EPRI data.

ACKNOWLEDGMENT

The authors would like to thank Boris Epel, Subramanian V. Sundramoorthy, Eugene Barth and Matt Maggio from The University of Chicago for providing the real data acquired from the 250MHz EPRI scanner.

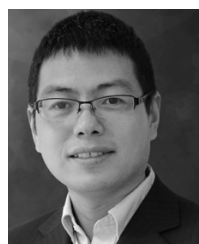
REFERENCES

- [1] B. Epel and H. Halpern, “Electron paramagnetic resonance oxygen imaging *in vivo*,” *Electron Paramagn. Reson.*, vol. 23, pp. 180–208, Nov. 2012.
- [2] B. Epel, M. Kotecha, and H. J. Halpern, “*In vivo* preclinical cancer and tissue engineering applications of absolute oxygen imaging using pulse EPR,” *J. Magn. Reson.*, vol. 280, pp. 149–157, Jul. 2017.
- [3] B. Epel, G. Redler, and H. J. Halpern, “How *in vivo* EPR measures and images oxygen,” *Adv. Exp. Med. Biol.*, vol. 812, p. 113, 2014.
- [4] H. M. Swartz, “The measurement of oxygen *in vivo* using EPR techniques,” *Phys. Med. Biol.*, vol. 43, no. 7, p. 1957, Mar. 1998.
- [5] Z. Qiao, G. Redler, B. Epel, and H. J. Halpern, “Comparison of parabolic filtration methods for 3D filtered back projection in pulsed EPR imaging,” *J. Magn. Reson.*, vol. 248, pp. 42–53, Nov. 2014.
- [6] Z. Qiao, G. Redler, B. Epel, Y. Qian, and H. Halpern, “3D pulse EPR imaging from sparse-view projections via constrained, total variation minimization,” *J. Magn. Reson.*, vol. 258, pp. 49–57, Sep. 2015.
- [7] K. I. Matsumoto, B. Chandrika, J. A. B. Lohman, J. B. Mitchell, M. C. Krishna, and S. Subramanian, “Application of continuous-wave EPR spectral-spatial image reconstruction techniques for *in vivo* oxymetry: Comparison of projection reconstruction and constant-time modalities,” *Magn. Reson. Med.*, vol. 50, no. 4, p. 865, 2003.
- [8] B. Epel, S. V. Sundramoorthy, E. D. Barth, C. Mailer, and H. J. Halpern, “Comparison of 250 MHz electron spin echo and continuous wave oxygen EPR imaging methods for *in vivo* applications,” *Med. Phys.*, vol. 38, no. 4, pp. 2045–2052, 2011.
- [9] B. Epel, S. V. Sundramoorthy, C. Mailer, and H. J. Halpern, “A versatile high speed 250-MHz pulse imager for biomedical applications,” *Concepts Magn. Reson. B, Magn. Eng.*, vol. 33, no. 3, pp. 163–176, 2008.
- [10] X. C. Pan, E. Y. Sidky, and M. Vannier, “Why do commercial CT scanners still employ traditional, filtered back-projection for image reconstruction?” *Inverse Problems*, vol. 25, no. 12, p. 123009, 2009.
- [11] K. T. Block, M. Uecker, and J. Frahm, “Undersampled radial MRI with multiple coils. Iterative image reconstruction using a total variation constraint,” *Magn. Reson. Med.*, vol. 57, pp. 1086–1098, Jun. 2007.
- [12] J. Bian, K. Yang, J. M. Boone, X. Han, E. Y. Sidky, and X. Pan, “Investigation of iterative image reconstruction in low-dose breast CT,” *Phys. Med. Biol.*, vol. 59, no. 11, pp. 2659–2685, 2014.
- [13] E. Y. Sidky, C.-M. Kao, and X. Pan, “Accurate image reconstruction from few-views and limited-angle data in divergent-beam CT,” *J. X-Ray Sci. Technol.*, vol. 14, no. 2, pp. 119–139, 2006.
- [14] J. Bian *et al.*, “Evaluation of sparse-view reconstruction from flat-panel-detector cone-beam CT,” *Phys. Med. Biol.*, vol. 55, no. 22, p. 6575, 2010.
- [15] J. Bian, J. Wang, X. Han, E. Y. Sidky, L. Shao, and X. Pan, “Optimization-based image reconstruction from sparse-view data in offset-detector CBCT,” *Phys. Med. Biol.*, vol. 58, no. 2, p. 205, 2012.
- [16] D. Xia *et al.*, “Optimization-based image reconstruction with artifact reduction in C-arm CBCT,” *Phys. Med. Biol.*, vol. 61, no. 20, pp. 7300–7333, 2016.
- [17] Z. Zhang, X. Han, E. Pearson, C. Pelizzari, E. Y. Sidky, and X. Pan, “Artifact reduction in short-scan CBCT by use of optimization-based reconstruction,” *Phys. Med. Biol.*, vol. 61, no. 9, p. 3387, 2016.
- [18] C. R. Vogel and M. E. Oman, “Iterative methods for total variation denoising,” *SIAM J. Sci. Comput.*, vol. 17, no. 1, pp. 227–238, 1996.
- [19] X. Han *et al.*, “Algorithm-enabled exploration of image-quality potential of cone-beam CT in image-guided radiation therapy,” *Phys. Med. Biol.*, vol. 60, no. 12, pp. 4601–4633, 2015.
- [20] Y. Ding and T. Hu, “Efficient scheme of low-dose CT reconstruction using TV minimization with an adaptive stopping strategy and sparse dictionary learning for post-processing,” *Frontiers Inf. Technol. Electron. Eng.*, vol. 18, no. 12, pp. 2001–2008, 2017.
- [21] Y. Sagara, A. K. Hara, W. Pavlicek, A. C. Silva, R. G. Paden, and Q. Wu, “Abdominal CT: comparison of low-dose CT with adaptive statistical iterative reconstruction and routine-dose CT with filtered back projection in 53 patients,” *AJR Amer. J. Roentgenol.*, vol. 195, no. 3, pp. 713–719, 2010.
- [22] Z. Zhang *et al.*, “Investigation of optimization-based reconstruction with an image-total-variation constraint in PET,” *Phys. Med. Biol.*, vol. 61, no. 16, p. 6055, 2016.
- [23] W. Bo, S. Boyd, M. Annergren, and Y. Wang, “An ADMM algorithm for a class of total variation regularized estimation problems,” *IFAC Proc.*, vol. 45, no. 16, pp. 83–88, 2012.
- [24] H. Nien and J. A. Fessler, “A convergence proof of the split Bregman method for regularized least-squares problems,” *Mathematics*, to be published.
- [25] A. Chambolle and T. Pock, “A first-order primal-dual algorithm for convex problems with applications to imaging,” *J. Math. Imag. Vis.*, vol. 40, no. 1, pp. 120–145, 2011.

- [26] E. Y. Sidky, J. H. Jørgensen, and X. Pan, "Convex optimization problem prototyping for image reconstruction in computed tomography with the Chambolle-Pock algorithm," *Phys. Med. Biol.*, vol. 57, no. 10, p. 3065, 2012.
- [27] K.-H. Ahn and H. J. Halpern, "Spatially uniform sampling in 4-D EPR spectral-spatial imaging," *J. Magn. Reson.*, vol. 185, no. 1, pp. 152–158, 2007.
- [28] E. Y. Sidky, D. N. Kraemer, E. G. Roth, C. Ullberg, I. S. Reiser, and X. Pan, "Analysis of iterative region-of-interest image reconstruction for X-ray computed tomography," *J. Med. Imag.*, vol. 1, no. 3, p. 031007, 2014.
- [29] Z. Qiao, G. Redler, Z. Gui, Y. Qian, B. Epel, and H. Halpern, "Three novel accurate pixel-driven projection methods for 2D CT and 3D EPR imaging," *J. X-Ray Sci. Technol.*, vol. 26, no. 1, pp. 83–102, 2018.
- [30] G. Redler, B. Epel, and H. J. Halpern, "Maximally spaced projection sequencing in electron paramagnetic resonance imaging," *Concepts Magn. Reson. B, Magn. Eng.*, vol. 45, no. 1, pp. 33–45, 2015.
- [31] B. Epel, I. Gromov, S. Stoll, A. Schweiger, and D. Goldfarb, "Spectrometer manager: A versatile control software for pulse EPR spectrometers," *Concepts Magn. Reson. B, Magn. Eng.*, vol. 26, no. 1, pp. 36–45, 2005.
- [32] L. I. Rudin, S. Osher, and E. Fatemi, "Nonlinear total variation based noise removal algorithms," *Phys. D, Nonlinear Phenomena*, vol. 60, nos. 1–4, pp. 259–268, 1992.
- [33] D. L. Donoho, "Compressed sensing," *IEEE Trans. Inf. Theory*, vol. 52, no. 4, pp. 1289–1306, Apr. 2006.
- [34] T. Chan, A. Marquina, and P. Mulet, "High-order total variation-based image restoration," *SIAM J. Sci. Comput.*, vol. 22, no. 2, pp. 503–516, 2001.
- [35] M. Lysaker and X.-C. Tai, "Iterative image restoration combining total variation minimization and a second-order functional," *Int. J. Comput. Vis.*, vol. 66, no. 1, pp. 5–18, 2006.
- [36] H. Kim, J. Chen, A. Wang, C. Chuang, M. Held, and J. Pouliot, "Non-local total-variation (NLTV) minimization combined with reweighted L1-norm for compressed sensing CT reconstruction," *Phys. Med. Biol.*, vol. 61, no. 18, pp. 6878–6891, 2016.
- [37] S. Ravishankar and Y. Bresler, "MR image reconstruction from highly undersampled k-space data by dictionary learning," *IEEE Trans. Med. Imag.*, vol. 30, no. 5, pp. 1028–1041, May 2011.
- [38] H. Chen *et al.*, "Low-dose CT with a residual encoder-decoder convolutional neural network," *IEEE Trans. Image Process.*, vol. 36, no. 12, pp. 2524–2535, Dec. 2017.
- [39] H. Chen *et al.*, "LEARN: Learned experts' assessment-based reconstruction network for sparse-data CT," *IEEE Trans. Med. Imag.*, vol. 37, no. 6, pp. 1333–1347, Jun. 2018.
- [40] H. Chen *et al.*, "Low-dose CT via convolutional neural network," *Biomed. Opt. Express*, vol. 8, no. 2, pp. 679–694, 2016.
- [41] G. Wang, "A perspective on deep imaging," *IEEE Access*, vol. 4, pp. 8914–8924, 2016.



ZHIWEI QIAO received the B.S. degree in information engineering, and the M.S. degree in computer science from the North University of China, Taiyuan, China, in 1999 and 2004, respectively, and the Ph.D. degree in transportation information engineering and control from Beijing Jiaotong University, Beijing, China, in 2011. He was a Visiting Scholar, and also a Postdoctoral Scholar of The University of Chicago, from 2012 to 2014. He is currently a Professor with the School of Computer and Information Technology, Shanxi University, Taiyuan, China, where he is also the Director of the China-USA United Lab for EPR Imaging. His research interests include image reconstruction algorithms and EPR imaging.



DONG LIANG received the Ph.D. degree in pattern recognition and intelligent systems from Shanghai Jiao Tong University, Shanghai, China, in 2006.

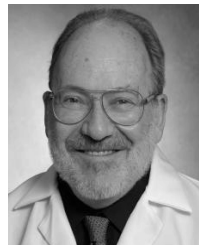
He was a Postdoctoral Researcher with The University of Hong Kong, from 2006 to 2007, and a Postdoctoral Researcher and Research Scientist with the University of Wisconsin-Milwaukee, from 2007 to 2011. He is currently a Professor with the Paul C. Lauterbur Research Center for Biomedical Imaging, Institute of Biomedical and Health Engineering, Shenzhen Institutes of Advanced Technology, Chinese Academy of Sciences, Shenzhen, China. His research interests include compressed sensing, image reconstruction, magnetic resonance imaging, and machine learning.

Dr. Liang is a Senior Member of the IEEE, and also a member of the ISMRM. He is an Associate Editor of the IEEE TRANSACTIONS ON MEDICAL IMAGING, and the Editorial Board Member of the *Magnetic Resonance in Medicine* and *Quantitative Imaging in Medicine and Surgery*.



SHAOJIE TANG received the Ph.D. degree in information and telecommunication engineering from Xi'an Jiaotong University, Xi'an, China, in 2010.

He was a Postdoctoral Scholar with Emory University, Atlanta, GA, USA, from 2010 to 2013. He is currently an Associate Professor with the School of Automation, Xi'an University of Posts and Telecommunications. His research interests include medical imaging, image processing, and computer vision.



HOWARD HALPERN received the Ph.D. degree in physics from Harvard University, in 1976, and the M.D. degree from the University of Miami, in 1980.

He is currently a Professor with the Department of Radiation and Cellular Oncology, The University of Chicago, Chicago, IL, USA, where he is also the Director of the NIH Center for EPR Imaging *in vivo* Physiology. His research interests include EPR imaging, radiation oncology, and physics in imaging sciences.